

Interfacial oxygen bridge bonding with Mo-O-Ti units in $\text{MoO}_x@\text{Ti}_3\text{C}_2$ MXene harness efficient Li-O₂ Battery at high rate

Zhihui Sun^a, Yingjie Hu^b, Jixiong Zhang^{a,*}, Nan Zhou^a, Meng Li^a, Hengfeng Liu^a, Binbin Huo^a, Ming Chao^{d,*}, Kai Zeng^{c,*}

^a School of Mines, China University of Mining and Technology, Xuzhou, Jiangsu 221116, China

^b Nanjing Key Laboratory of Advanced Functional Materials, Nanjing Xiaozhuang University, Nanjing, Jiangsu 211171, China

^c Institute of Smart City and Intelligent Transportation, Southwest Jiaotong University, Chengdu 610032, China

^d College of Energy, Soochow Institute for Energy and Materials Innovation, Soochow University, Suzhou 215006, China



ARTICLE INFO

Keywords:

Li-O₂ battery
MXene
Interfacial oxygen bridge bonding
Electronic structure

ABSTRACT

The rational pursuit of competent bifunctional catalysts for facilitating oxygen redox kinetics is critical in boosting the Li-O₂ battery commercial application. Here, we report the preparation of efficient $\text{MoO}_x@\text{Ti}_3\text{C}_2$ MXene catalysts with optimized electronic structure by in-situ incorporation of interfacial oxygen bridge bonding with Mo-O-Ti units. $\text{MoO}_x@\text{Ti}_3\text{C}_2$ MXene delivers tailored chemical bonding, amplified electrical conductivity, and outstanding high-rate stability. The as-constructed $\text{MoO}_x@\text{Ti}_3\text{C}_2$ MXene-based Li-O₂ battery achieves lower discharge/charge polarization of 0.75 V and long-term lifespan of 300 hours (over 300 cycles) under 2500 mA g⁻¹, exceeding those of reported related catalysts. Density functional theory analysis and ex-situ experiments reveal the critical role of bimetallic-oxygen coupling in regulating the micro-chemical constitution and controlling the Li_2O_2 formation mode. This work could provide consideration insights in the rational design of competent and stable MXene-based cathode catalyst with bimetallic heterostructure for high-rate Li-O₂ batteries.

1. Introduction

Li-O₂ batteries (LOBs) have knocked on a new electrochemical avenue to meet the growing demand for energy storage owing to their ultra-high theoretical energy density and prospective air-based raw-reactant [1]. However, semi-open fabric and sluggish oxygen redox kinetics of LOBs have attracted high overpotential, unsatisfied rate capability, and poor lifespan, which in turn restricting further practical commercialization [2]. The cathode electrocatalysts with distinctive architecture manufacturing and sufficient electrochemical activity are considered to be the trump card for solving those aforementioned problems in metal-oxygen batteries [3,4]. Various cathode electrocatalysts have been thoroughly explored to facilitate the dynamics of the oxygen reduction reaction (ORR) and oxygen evolution reaction (OER) [5,6]. Despising the high activation in regulating the formation/decomposition pathways of product, noble metals with half-filled antibonding are limited by expensive costs and difficult structural regulation [7,8]. Featured with high stability and adjustable microstructure, transition metal oxides deliver poor catalytic selectivity

for oxygen redox, leading to poor electrochemical performance [9–11]. Single-atom catalysts with unique active sites and electronic properties are restricted by the tedious synthesis process and inferior structural stability [12–14]. Carbonaceous materials suffer from nucleophilic attack of reactive oxygen species, resulting to a series of side reactions [15,16].

Transition metal carbides (MXenes) have been wildly confirmed to deliver tremendous catalytic activity for OER and ORR [17,18]. MXenes is armed with rich active termination, which could optimize their charge density and intern expanding electronic properties [19,20]. For example, MXene with controllable d-spacing show efficient charge transportation and electrochemical activity to accelerate reaction kinetics in rechargeable battery [21]. In addition, in-situ fabricated transitional metal oxide-based surface on MXene could make difference in shorting ion diffusion and promoting redox dynamic [22,23]. Moreover, MXene have a unique 2D graphene-like structure, which modifies the formation/decomposition path of Li_2O_2 and induces homogeneous Li_2O_2 deposition in LOBs [24,25]. Unfortunately, MXene flakes tend to be oxide and restacked at anodic potentials, leading to active sites

* Corresponding authors.

E-mail addresses: cumtzjxiong@163.com (J. Zhang), 779187999@qq.com (M. Chao), zengkai@swjtu.edu.cn (K. Zeng).

inaccessible and unpromising by-product nucleation [26].

Molybdenum oxides have electronic structure of coexisting multi-valent states rich and high electronegativity characteristics [27]. In detail, MoO_2 with rich Mn^{3+} and Mn^{5+} delivers rich oxygen vacancy and thereby enhanced bifunctional catalytic activity to ORR/OER [28]. N-doped MoO_2 is exceptional active sites to heighten the adsorption of LiO_2 and to attract the following uniform growth of Li_2O_2 in LOBs [29]. On the other hand, Molybdenum oxides-based compounds provide heterojunction for accelerated electronic distribution and altered chemical stability in high rate of LOBs [30,31]. Nevertheless, Molybdenum oxides suffer from low conductivity and limited catalytic selectivity to Li_2O_2 decomposition [32]. Besides, the erratic precipitation of dielectric Li_2O_2 will choke the catalysis sites of molybdenum oxides and inferior charging performance, eventually leading to raising polarization during long lifespan [33].

Herein, a stable bimetallic-oxygen coupling was fabricated by the strong self-assembly of MoO_x and Ti_3C_2 MXene. The combination of Mo (derived from MoO_x) and TiO_2 (active termination of Ti_3C_2) resulted in a bimetallic Mo/Ti-O bonding with an optimized interface electronic structure, qualified chemical stability, and bifunctional oxygen redox facilitation as the cathode catalyst. LOBs with $\text{MoO}_x@\text{Ti}_3\text{C}_2$ MXene-based cathode show lower voltage polarization of 0.75 V, long-term lifespan for 300 hours (about 300 cycles), and exceed rate performance at 2500 mA g⁻¹, showing better electrochemical performance than that of monoclinic related catalysts. Moreover, the key influence of bimetallic-oxygen coupling in facilitating the ORR/OER dynamics and optimizing the adsorption/desorption of Li_2O_2 was deeply investigated by experimental and theoretical analysis.

2. Experimental section/methods

2.1. Synthesis of Ti_3C_2 MXene

2 g Lithium fluoride (LiF) powder was added into 40 mL hydrogen chloride (9 M) solution under magnetic stirring for 0.5 h at room temperature to generate hydrofluoric acid solution (HF). Then, 2.0 g Ti_3AlC_2 MAX powder was added slowly into 50% HF for 1 h at 40 °C under vigorous stirring. The mixture was transferred and sealed into 100 mL Teflon-lined hydrothermal autoclave and heated at 90 °C for 20 hrs. The product was centrifuged with deionized water and ethanol at 8000 rpm for 4–5 times until the pH value was adjusted to ~7 while removing excess impurities. Finally, the collected precipitation was dried at 60 °C and was calcined at 350 °C for 2 hrs to obtain desirable Ti_3C_2 MXene.

2.2. Synthesis of $\text{MoO}_x@\text{Ti}_3\text{C}_2$ MXene

0.5 g $(\text{NH}_4)_6\text{Mo}_7\text{O}_{24}\cdot 4\text{H}_2\text{O}$ and 0.125 g glucose were respectively dissolved in 60 mL ultrapure water with continuous physical stirring. Then, 0.1 g prefabricated Ti_3C_2 MXene was added into the above dispersion with continuous physical stirring. Then, the homogeneous solution was transferred and sealed into 100 mL Teflon-lined hydrothermal autoclave and heated at 180 °C for 12 h. The resultant mixture was washed by centrifuged with deionized water and ethanol to obtain precursor. Finally, the precursor was calcined at 750 °C for 4 h under Ar atmosphere with a heating rate of 5 °C min⁻¹ to form $\text{MoO}_x@\text{Ti}_3\text{C}_2$ MXene. The MoO_x nanoparticles were obtained by Hydrothermal reaction without the addition of Ti_3C_2 MXene under the same conditions as above. For comparison, $\text{MoO}_x@\text{Ti}_3\text{C}_2$ MXene-1 was also synthesized by the similar procedures with just change the mass of $(\text{NH}_4)_6\text{Mo}_7\text{O}_{24}\cdot 4\text{H}_2\text{O}$ to 0.25 g. Furthermore, $\text{MoO}_x@\text{Ti}_3\text{C}_2$ MXene-2 was synthesized by the similar procedures with just change the mass of $(\text{NH}_4)_6\text{Mo}_7\text{O}_{24}\cdot 4\text{H}_2\text{O}$ to 0.75 g.

2.3. Cathode preparation and measurement

The catalyst materials ($\text{MoO}_x@\text{Ti}_3\text{C}_2$ MXene, MoO_x , Ti_3C_2 MXene),

conductive additive (acetylene black), and binder (polyvinylidene fluoride, PVDF) were weighed in a mass ratio of 7:2:1. After mixing and grinding, the mixture was dissolved in N-Methyl pyrrolidone and stirred for 12 hours to form a thick and uniform slurry. Then, the prepared slurry was coated onto the carbon paper and dried at 60°C. Finally, the catalyst-based cathode with loading of ~0.6 mg cm⁻² was cut into a disk ($\phi = 12$ mm).

The 2032 coin-type LOBs were assembled in a glovebox with as-prepared cathode, Li metal anode, glass microfiber diaphragm (Grade GF/D), and electrolyte (1.0 M lithium bis (trifluoromethane sulfonyl) imide dissolved in dimethyl sulfoxide). The assembled LOBs are placed in a self-made glass bottle (Figure. S1) sealed with oxygen. The performance measurement of LOBs was conducted by the Blue Electric Battery Testing System (LANHE CT3001A) of Wuhan Blue Electric Company.

3. Results and discussion

3.1. Morphological and structural characterization

As shown in Fig. 1a and Figure S2, the diffraction pattern of typical Ti_3C_2 MXene deliver no characteristic peaks indicative of crystalline phases. Wide-angle X-ray diffraction of MoO_x catalyst exhibits significant peaks at 26.1°, 37.1°, 54.5°, 60.1° and 66.7°, which are characteristic of monoclinic MoO_2 (JCPDF: #32-0671). By comparison, the pattern for $\text{MoO}_x@\text{Ti}_3\text{C}_2$ MXene could be well-indexed to MoO_2 . Besides, the enlarge contour XRD patterns further showed that the broad peaks of $\text{MoO}_x@\text{Ti}_3\text{C}_2$ MXene were sharply shifted to the small angle, which is mainly related to a larger lattice spacing caused by Ti-interaction. The FT-IR spectra of Ti_3C_2 MXene (Figure. S3) shows C=C bond, C-H groups, and Ti-O bond at 1629, 837, and 550 cm⁻¹, respectively. Ti-O bond confirm the in-situ fabricated transitional metal oxide-based surface on Ti_3C_2 MXene, which could serve as active sites for shortened ion diffusion and fast redox reactions. These C-H groups have been reported to be easily reacted with Mo into Mo_2C under the calcination process with Ar atmosphere [34]. By comparison, the presence of Mo/Ti-O stretching vibration in $\text{MoO}_x@\text{Ti}_3\text{C}_2$ MXene reveals bimetallic oxide active sites are stably manufactured on $\text{MoO}_x@\text{Ti}_3\text{C}_2$ MXene. The Raman spectra in Fig. 1b was conducted to investigate the molecular interactions features and chemical structural of as-prepared catalysts. Interestingly, MoO_x and $\text{MoO}_x@\text{Ti}_3\text{C}_2$ MXene illustrate similar and weak Mo-C vibration peaks located at 993 cm⁻¹, indicating that the surface carbonization of molybdenum oxide [35]. The I_D/I_G ratio deliver no obvious change between MoO_x and $\text{MoO}_x@\text{Ti}_3\text{C}_2$, showing that the carbon residue share similar crystallinity and dense defects sites. Fig. 1c and Figure S4 show the interfaces between MoO_x and TiO_x (in-situ formed active layer on Ti_3C_2 MXene) by DFT calculations. The interfacial oxygen bridge bonding with Mo and Ti could influence the coordination environment of both MoO_x and TiO_x , leading to the enhanced chemical stability of $\text{MoO}_x@\text{Ti}_3\text{C}_2$ MXene.

High-magnification SEM image in Fig. 1d shows that the as-deposited MoO_x nanosheets are randomly distributed on the Ti_3C_2 MXene surface. By comparison, Ti_3C_2 MXene exhibits smooth multi-layer nanosheet structure and monoclinic MoO_x delivers stacked nanoparticle morphology, indicating the bimetallic-oxygen coupling could regulating the morphology of MoO_x and inhibiting the aggregation of MoO_x nanostructures. Besides, the content of molybdenum precursor will affect the loading of MoO_x on the Ti_3C_2 MXene, and the $\text{MoO}_x@\text{Ti}_3\text{C}_2$ MXene shows the best optimal structure. The in-depth multicomponent heterostructure of $\text{MoO}_x@\text{Ti}_3\text{C}_2$ MXene was investigated by TEM analysis. Low-resolution TEM image in Fig. 1e delivers that the synthesized MoO_x nanosheets with roughly 170 nm in diameters are developed from cluster nanoparticles core, forming coral-like protective-layer over MXene hosts. In more detail, Fig. 1f exhibits an apparently multiphase coexisting structure with amorphous and crystalline phase in $\text{MoO}_x@\text{Ti}_3\text{C}_2$ MXene. In addition, the $\text{MoO}_x@\text{Ti}_3\text{C}_2$ MXene reveals the characteristic spacing of 0.344 and 0.244 nm for the

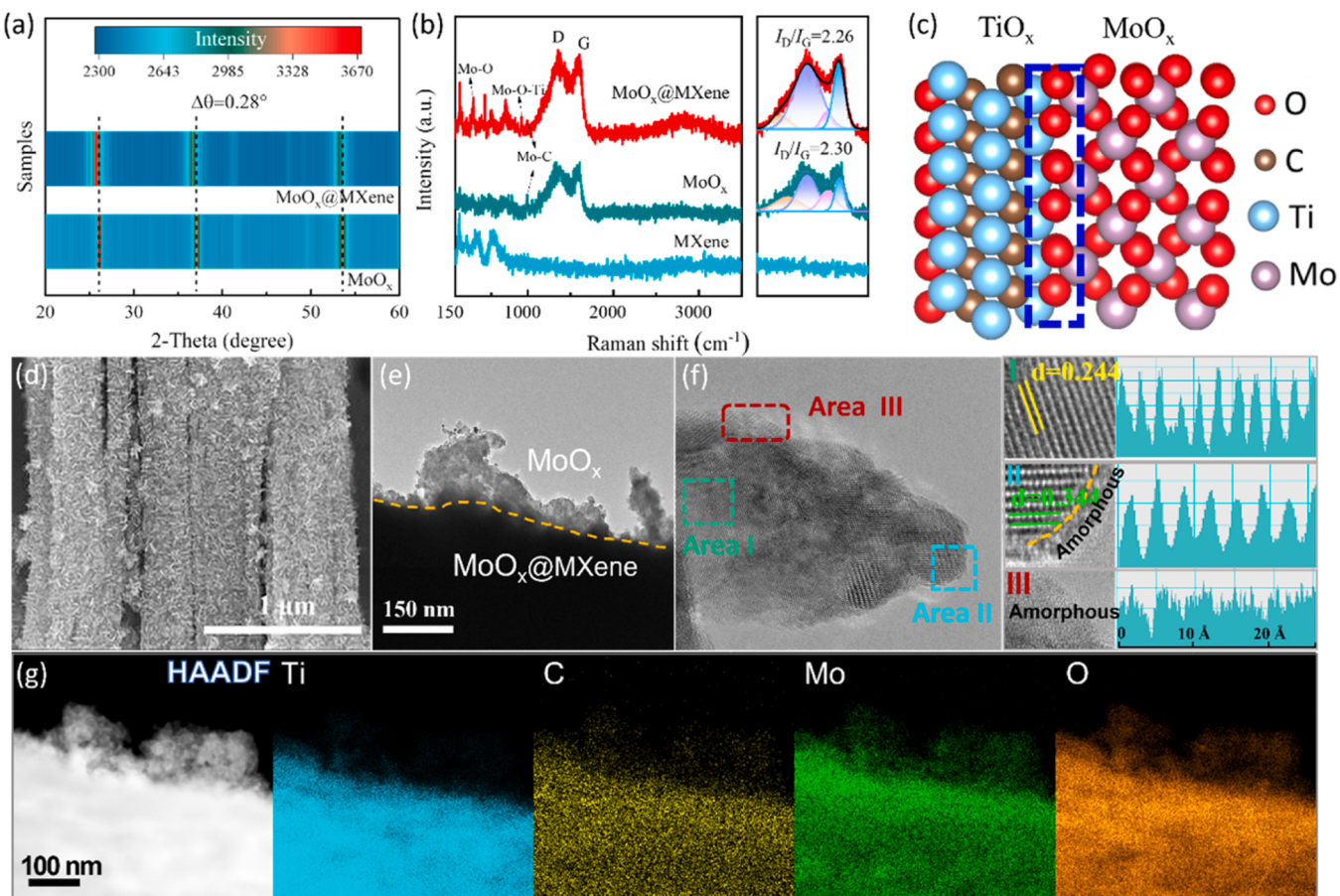


Fig. 1. XRD patterns (a) and Raman spectrum (b) of as-prepared samples; (c) Schematic model of optimized Mo-O-Ti heterostructure in $\text{MoO}_x@\text{Ti}_3\text{C}_2$ MXene; SEM image (d) TEM image (e) HR-TEM image (f) and EDS mapping images (g) of $\text{MoO}_x@\text{Ti}_3\text{C}_2$ MXene.

(-111) and the (-211) lattice planes of MoO_x , which is larger than that of MoO_x (0.342 and 0.242 nm for the (-111) and the (-211) lattice planes, accordingly). This phenomenon provides further evidence to successful doping of heteroatomic Ti with large atomic radius, which is well corroborated with previous XRD analysis. Moreover, the enlarged pattern of area II shows that there is a distinct amorphous/crystalline coexisting region between MoO_x and Ti_3C_2 MXene. The atomic-resolution HAADF images of the $\text{MoO}_x@\text{Ti}_3\text{C}_2$ MXene in Fig. 1g reveal that the as-prepared catalyst display a uniform mixture of Ti, C, Mo and O. Impressively, there is unobservable distribution of Ti atoms in the coral-like protective-layer, revealing that the coral-like protective-layer is composed of MoO_x . Moreover, the presence of a few carbon in the protective layer confirm the existence of molybdenum carbide, ting well with previous Raman studies wherein the partial carbonization of MoO_x .

Ulteriorly, the composition difference among MoO_x , Ti_3C_2 MXene, and $\text{MoO}_x@\text{Ti}_3\text{C}_2$ MXene were additionally explored by XPS and XAFS. The full spectrum of $\text{MoO}_x@\text{Ti}_3\text{C}_2$ MXene demonstrates the existence of C, Ti, O, and Mo elements (Figure S6). The refined Ti 2p spectra of Ti_3C_2 MXene (Fig. 2a) show seven intense peaks at 464.92, 462.62, 461.08, 459.27, 457.47, 455.66 and 454.61 eV, associated with the Ti–O ($\text{Ti} 2p_{1/2}$), Ti^{2+} ($\text{Ti} 2p_{1/2}$), Ti–C ($\text{Ti} 2p_{1/2}$), Ti–O ($\text{Ti} 2p_{3/2}$), Ti^{2+} ($\text{Ti} 2p_{3/2}$), Ti–O–C ($\text{Ti} 2p_{3/2}$), and Ti–C ($\text{Ti} 2p_{3/2}$), respectively. In contrast, $\text{MoO}_x@\text{Ti}_3\text{C}_2$ MXene shows only two strong peaks related to Ti–O bonding, derived from the in-situ formation of titanium oxide protective layer. By thorough comparison, a slight downshift (0.2 eV) for $\text{MoO}_x@\text{Ti}_3\text{C}_2$ MXene was observed, owing to the strong interaction between Ti and Mo [36]. The refined C 1s spectrum of Ti_3C_2 MXene (Fig. 2b) could be well divided into four characteristic peaks: C=C=O (288.92 eV), C–O (286.02 eV), C–C (284.80 eV), and C–Metal Ti

(281.78 eV), separately. Notably, the C–Metal bonding (282.16 eV) in $\text{MoO}_x@\text{Ti}_3\text{C}_2$ MXene are significant upshifting, while weaker than that of Ti_3C_2 MXene. The extraordinary chemical state changing could be attributed to the microcosm interference of simultaneously formation of molybdenum carbide and titanium oxide. From the Fig. 2c, the O 1s spectrum for Ti_3C_2 MXene is divided into two features at 530.52 (O–Ti) eV and 531.66 eV (defected oxygen, abbreviated as Ov), in-depth proofing the existence of titanium oxide [37]. Furthermore, the characteristic peak of O–Metal bonding in $\text{MoO}_x@\text{Ti}_3\text{C}_2$ MXene upshifts to Ti_3C_2 MXene, meanwhile showing smaller than that of MoO_x , corresponds to Ti–O–Mo bonds, implying the formation of heterointerface between MXene and MoO_x . The electron paramagnetic resonance (EPR) was further conducted to character the Ov. As shown in Figures S7, wherein the Ov– MoO_x and Ov– $\text{MoO}_x@\text{Ti}_3\text{C}_2$ MXene exhibited signals at $g = 2.003$ induced by the Ov formation. Moreover, the lattice oxygen is released from the crystal surface to form abundant oxygen defects and leave unpaired electrons, resulting in a high-intensity EPR signal. The stronger intensity of Ov initially in $\text{MoO}_x@\text{Ti}_3\text{C}_2$ MXene indicates that the presence of interfacial oxygen bridge bonding with Mo–O–Ti units could introduce more Ov on the surface of whole hybrid. As shown in Fig. 2d, the Mo 3d orbital for $\text{MoO}_x@\text{Ti}_3\text{C}_2$ MXene is deconvoluted into five features, related to the Mo^{6+} (236.05 and 233.02 eV), Mo^{5+} (234.6 eV), Mo^{4+} (231.63 eV), and Mo^{3+} (229.73 eV), respectively [38]. Comparatively, the Mo 3d spectrum of $\text{MoO}_x@\text{Ti}_3\text{C}_2$ MXene slightly offset toward high binding energy (~ 0.16 eV, owing to the strong interactions between Ti atoms with smaller electronegative. Additionally, the raising non nominal titanium oxide of Mo (5+, 3+) in $\text{MoO}_x@\text{Ti}_3\text{C}_2$ MXene are wildly considered to be the main active sites in promoting the electron transfer for ORR and OER, leading to enhanced

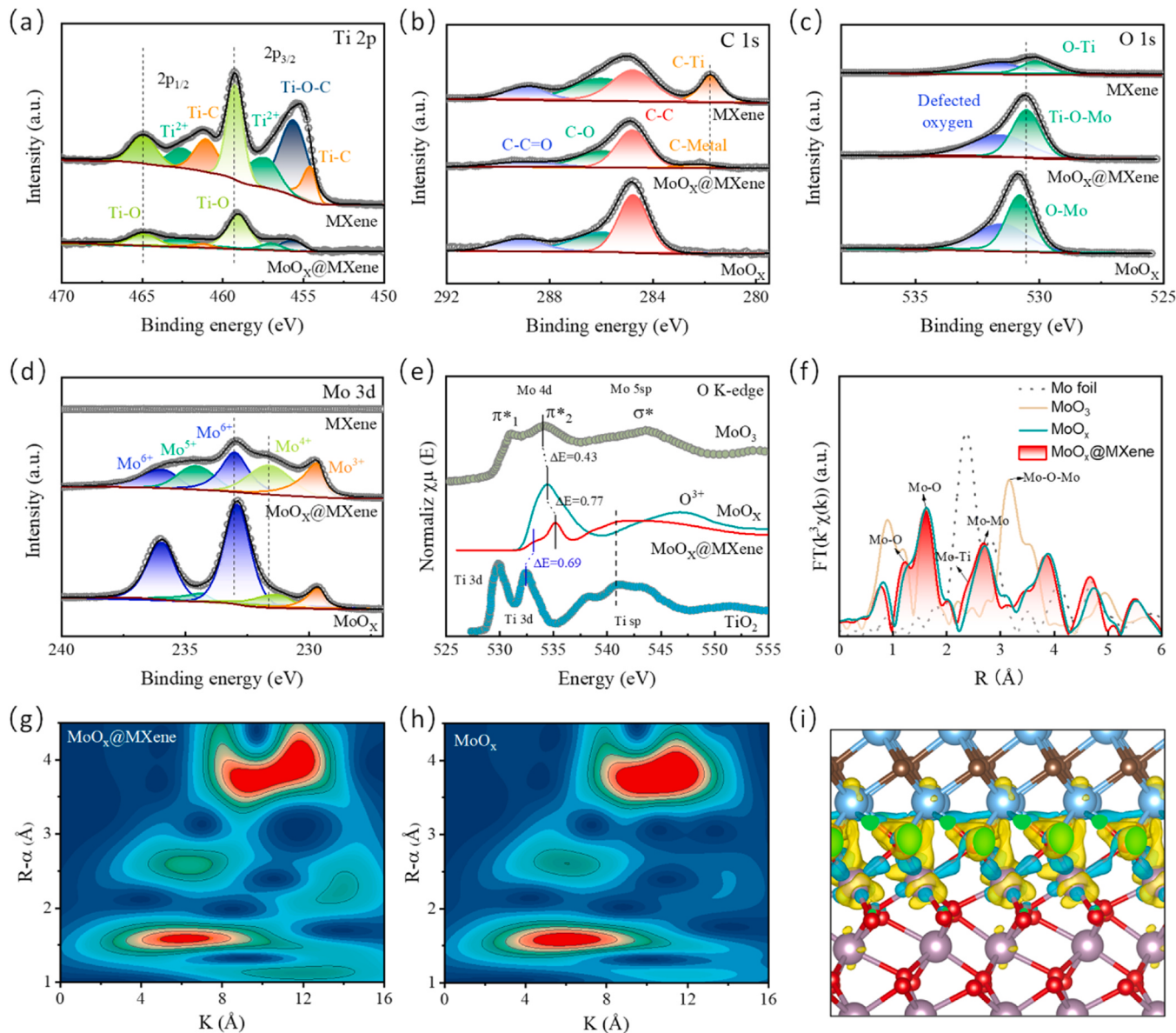


Fig. 2. High-resolution Ti 2p (a), C 1 s (b), O 1 s (c), and Mo 3d (d) spectra for various catalysts; (e) Oxygen K-edge spectra of MoO_3 , MoO_x , Ti_3C_2 MXene, and $\text{MoO}_x@\text{Ti}_3\text{C}_2$ MXene; (f) Radial distribution functions of as-prepared catalysts obtained from the $k^2\chi(k)$ by Fourier transform (FT); Wavelet transform (WT) contour plots of $\text{MoO}_x@\text{Ti}_3\text{C}_2$ MXene (g) and MoO_x (h); (i) Charge density difference plots of primal MoO_x (010) and Ti_3C_2 (001), with yellow denoting the increased charge and cyan the decreased charge (the green area represents the cross section of CDD at periodic boundary condition).

catalytic performance in LOBs.

To further explore the bimetallic-oxygen coupling mechanism of $\text{MoO}_x@\text{Ti}_3\text{C}_2$ MXene, synchrotron radiation analysis was conducted. According to the O K-edge XAFS spectrum in Fig. 2e, MoO_3 shows an obvious peaks at 535 eV, which could be assigned to the $\pi^*(2\text{b}_1) \leftarrow \text{ls}$ (2a_1) resonance excitation of the centra O atom [39]. Narrowly, the energy at the π^*_2 absorption edge in $\text{MoO}_x@\text{Ti}_3\text{C}_2$ MXene is distinctly higher (536 eV), implying the transitions to the σ^* (7a_1) $\leftarrow \text{ls}$ ($2\text{a}_1/1\text{b}_2$) level from the terminal O atom. Besides, the broad peak centra at 541 eV in $\text{MoO}_x@\text{Ti}_3\text{C}_2$ MXene could be attributed to the 4sp TiO_2 , indicating the elements substitution for Ti replaces the Mo 5sp states and accordingly strengthening the first structure in the oxygen K-edge. As displayed in the Mo K-edge XAFS spectrum, $\text{MoO}_x@\text{Ti}_3\text{C}_2$ MXene delivers difference-blind features to that of MoO_x , but absorption edge upset to lower energy, implying an increase in low valence of Mo in $\text{MoO}_x@\text{Ti}_3\text{C}_2$ (Figure S8) [40]. Furthermore, the extended X-ray absorption fine structure (EXAFS) spectra is adopt to in-depth investigate the atomic

spacing and coordination of Mo in $\text{MoO}_x@\text{Ti}_3\text{C}_2$ MXene and MoO_x (Fig. 2f). The Fourier transform (FT) curve of both $\text{MoO}_x@\text{Ti}_3\text{C}_2$ MXene and MoO_x present two characteristic peaks located at ~ 1.59 and 2.69 Å, which are indexed well with Mo-O and Mo-Mo bonds, respectively. In addition, $\text{MoO}_x@\text{Ti}_3\text{C}_2$ MXene shows negligible Mo-O-Mo (3.15 Å) coordination and emerging Mo-Ti bond (2.37 Å) regarding to MoO_x and MoO_3 , suggesting the strong interactions between Mo and Ti [41]. The WT contour plot of $\text{MoO}_x@\text{Ti}_3\text{C}_2$ MXene exhibits two maximal centers at ~ 6.12 and 9.4 Å, corresponding to Mo-O and Mo-Metal (Fig. 2g). Besides, The WT contour plot of MoO_x exhibits two maximal centers at ~ 6.3 and 10.34 Å, corresponding to Mo-O and Mo-Mo (Fig. 2h). The offset centers of Mo-O and Mo-Metal in $\text{MoO}_x@\text{Ti}_3\text{C}_2$ MXene is attributed to the formation of bimetallic Mo-O-Ti coupling. Furthermore, the charge density difference was calculated to distinctly analyze the charge variation in $\text{MoO}_x@\text{Ti}_3\text{C}_2$ MXene (Fig. 2i). The DFT analysis reveals that the (010) lattice planes MoO_x delivers negligible mismatch and dislocations to the (001) lattice planes of Ti_3C_2 , resulting to Mo atom preferentially

bond with O from TiO_x active layer on Ti_3C_2 MXene and thereby to enhance the electronegativity of Mo centers. In detail, When Mo atom is combined with oxygen atoms from TiO_x active layer on Ti_3C_2 MXene, bigger charged areas are mainly observed between Mo site and O atoms than that between Ti site and O atoms (marked in yellow). The DFT results is consistent with previous XPS analysis, indicates that the bimetallic Mo-O-Ti coupling is fabricated by the favourable bonding between foreign Mo atom and TiO_x active layer.

3.2. 2032-coin $\text{Li}-\text{O}_2$ battery performance

The electrocatalytic performance of $\text{MoO}_x@\text{Ti}_3\text{C}_2$ MXene is evaluated via the assembled 2032-coin LOBs. The whole operating mechanism of LOBs is vividly described in Fig. 3a. External oxygen can interact with Lithium-ion (diffused from the anode) to grow up Li-based products on the cathode during discharging, which is completely degraded after the subsequent charging. The catalyst-decorated cathode plays a major dual-role as an electrochemical reaction electrode and a storage/decomposition area for the product in LOBs. Accordingly, the activity of cathode catalyst makes critical difference in boosting the practical efficiency of LOBs. It should be noted that, as shown in the Figure S9a, the LOBs with monomer MoO_x catalyst can only sustain stably for one charge-discharge cycle at high rate, indicating that MoO_x could not exhibit stable catalytic activity at ultra-high rate. As shown in Figure S9b, the surface of MoO_x particles was fully deposited with film products after the 1st charge under a high rate. XPS spectrum of Li 1 s in

Figure S9c further reveal that the film products formed on the MoO_x cathode is mainly the indecomposable Li_2CO_3 . The unsatisfied Li_2CO_3 passivation layer can mask the active sites of MoO_x and prevent the following catalytic reaction during the charging process. This could reveal that MXene act as protective layers to improve the structural and property stability of whole matrix. Therefore, in subsequent experiments, no further analysis or testing will be conducted on MoO_x -based LOBs. As shown in the cyclic voltammetry (CV) curves (Fig. 3b), $\text{MoO}_x@\text{Ti}_3\text{C}_2$ MXene demonstrates a higher ORR onset potential (2.89 V) and lower OER onset potential of 3.30 V, demonstrating the best ORR/OER bifunctional catalytic activity. Specifically, $\text{MoO}_x@\text{Ti}_3\text{C}_2$ MXene appears bigger anodic peak area, suggesting a bigger specific capacity. The CV results indicates that $\text{MoO}_x@\text{Ti}_3\text{C}_2$ MXene has a promising bifunctional oxygen catalytic performance. The in-situ incorporation of interfacial oxygen bridge bonding with Mo-O-Ti units in $\text{MoO}_x@\text{Ti}_3\text{C}_2$ MXene could provide faster charge transfer channels and higher electrocatalytic activity in oxygen reactions. As presented in Fig. 3c, $\text{MoO}_x@\text{Ti}_3\text{C}_2$ MXene delivers a higher discharge specific capacity of 7819 mAh g^{-1} than Ti_3C_2 MXene (7164 mAh g^{-1}) at a striking current density of 2500 mA g^{-1} . Besides, $\text{MoO}_x@\text{Ti}_3\text{C}_2$ MXene exhibits lower polarization overpotential of 1.28 V than Ti_3C_2 MXene (1.51 V), signifying the acceleration of ORR/OER kinetics and inhibition of organic electrolyte decomposition, which is consistent with the previous CV analysis. The endurance stability of LOBs with catalysts (Fig. 3d) are tested under the galvanostatic condition of 2500 mA g^{-1} with a cut-off capacity of 1000 mAh g^{-1} . The LOBs with $\text{MoO}_x@\text{Ti}_3\text{C}_2$ MXene

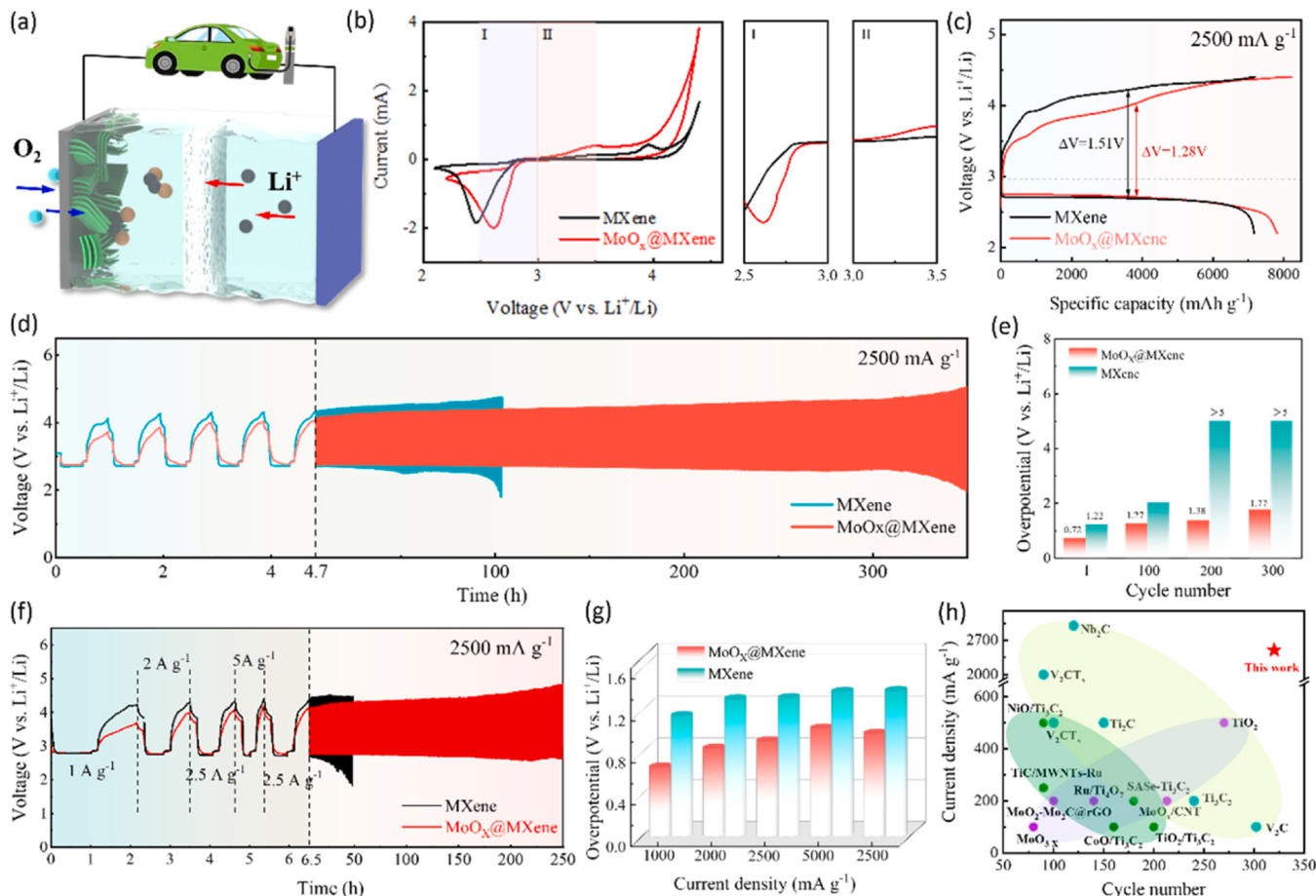


Fig. 3. (a) Working mechanism of LOBs with $\text{MoO}_x@\text{Ti}_3\text{C}_2$ MXene-based cathode; (b) CV curves at a scan rate of 0.1 mV s^{-1} within a voltage window of 2.2 – 4.4 V ; (c) Initial full discharge/charge curves of as-prepared catalysts-based LOBs at 2500 mA g^{-1} ; (d) Discharge/charge cycling stability of as-prepared catalysts-based LOBs at a current density of 2500 mA g^{-1} with a cut-off capacity of 1000 mAh g^{-1} ; (e) The overpotential of $\text{MoO}_x@\text{Ti}_3\text{C}_2$ MXene and MXene at different cycling; (f) Rate performances of catalysts-based LOBs at different discharge/charge current densities; (g) The overpotential of $\text{MoO}_x@\text{Ti}_3\text{C}_2$ MXene and MXene at different current densities; (h) Comparisons in the performance of LOBs based on $\text{MoO}_x@\text{Ti}_3\text{C}_2$ MXene and other reported electrocatalysts.

catalyst-based cathode could stably sustain over 300 hrs without distinct performance degradation at ultrahigh rate, whereas the cathode loaded with Ti_3C_2 MXene could only maintain 100 hrs along with severe voltage polarization. By comparison, the cycling stability of LOBs with catalysts (Figure S10) are also tested under the galvanostatic condition of 1000 mA g^{-1} and 3000 mA g^{-1} with a cut-off capacity of 1000 mAh g^{-1} . The LOBs with $\text{MoO}_x@\text{Ti}_3\text{C}_2$ MXene catalyst-based cathode could stably sustain over 350 hrs without distinct performance degradation at 1000 mA g^{-1} , whereas the cathode loaded with Ti_3C_2 MXene could only maintain 150 hrs along with severe voltage polarization. Moreover, The LOBs with $\text{MoO}_x@\text{Ti}_3\text{C}_2$ MXene catalyst-based cathode could stably sustain about 125 hrs at 3000 mA g^{-1} , whereas the cathode loaded with Ti_3C_2 MXene could only maintain 80 hrs along with severe voltage polarization. Accordingly, The LOBs with $\text{MoO}_x@\text{Ti}_3\text{C}_2$ MXene catalyst-based cathode could deliver excellent cyclic stability at both low and high rate. The existence of interfacial oxygen bridge bonding with Mo-O-Ti units could promote the catalytic activity of monomer Ti_3C_2 MXene, which further increases the total charge-discharge capacity of $\text{Li}-\text{O}_2$

battery. As clearly demonstrated in Fig. 3e and Figure S11, the $\text{MoO}_x@\text{Ti}_3\text{C}_2$ MXene-based cathode delivers the lower discharge/charge polarization of 0.75 V at the 1st cycle compared to Ti_3C_2 MXene cathode (1.22 V), and MoO_x (1.58 V), respectively. Moreover, the swift declining discharge terminal voltage and rapid raising charge median voltage of MoO_x -based cathode after 100 hrs charge/discharge cycling give valid evidence to the low ORR/OER activity and the limited stability of the oxide monomer-based catalyst in ultrahigh rate of 2500 mA g^{-1} . Meanwhile, the Ti_3C_2 MXene-based cathode shows an increased discharge-charge overpotential from 1.22 V (1st cycle) to 2.03 V (100th cycle), followed to death immediately. Impressively, the $\text{MoO}_x@\text{Ti}_3\text{C}_2$ MXene cathode with bimetallic active sites (Mo and Ti) provides a low overpotential (1.38 V at 200 cycles) and prominent cyclic stability (over 300 cycles). The rate capacity curve of $\text{MoO}_x@\text{Ti}_3\text{C}_2$ MXene catalyst in Fig. 3f demonstrates a marginal difference under different current densities ranging from 1 to 5 A g^{-1} . In detail, $\text{MoO}_x@\text{Ti}_3\text{C}_2$ MXene maintains a stable discharge-charge overpotential from $\sim 0.66 \text{ V}$ (1000 mA g^{-1}) to $\sim 1.03 \text{ V}$ (5000 mA g^{-1}) and $\sim 0.98 \text{ V}$ (upon

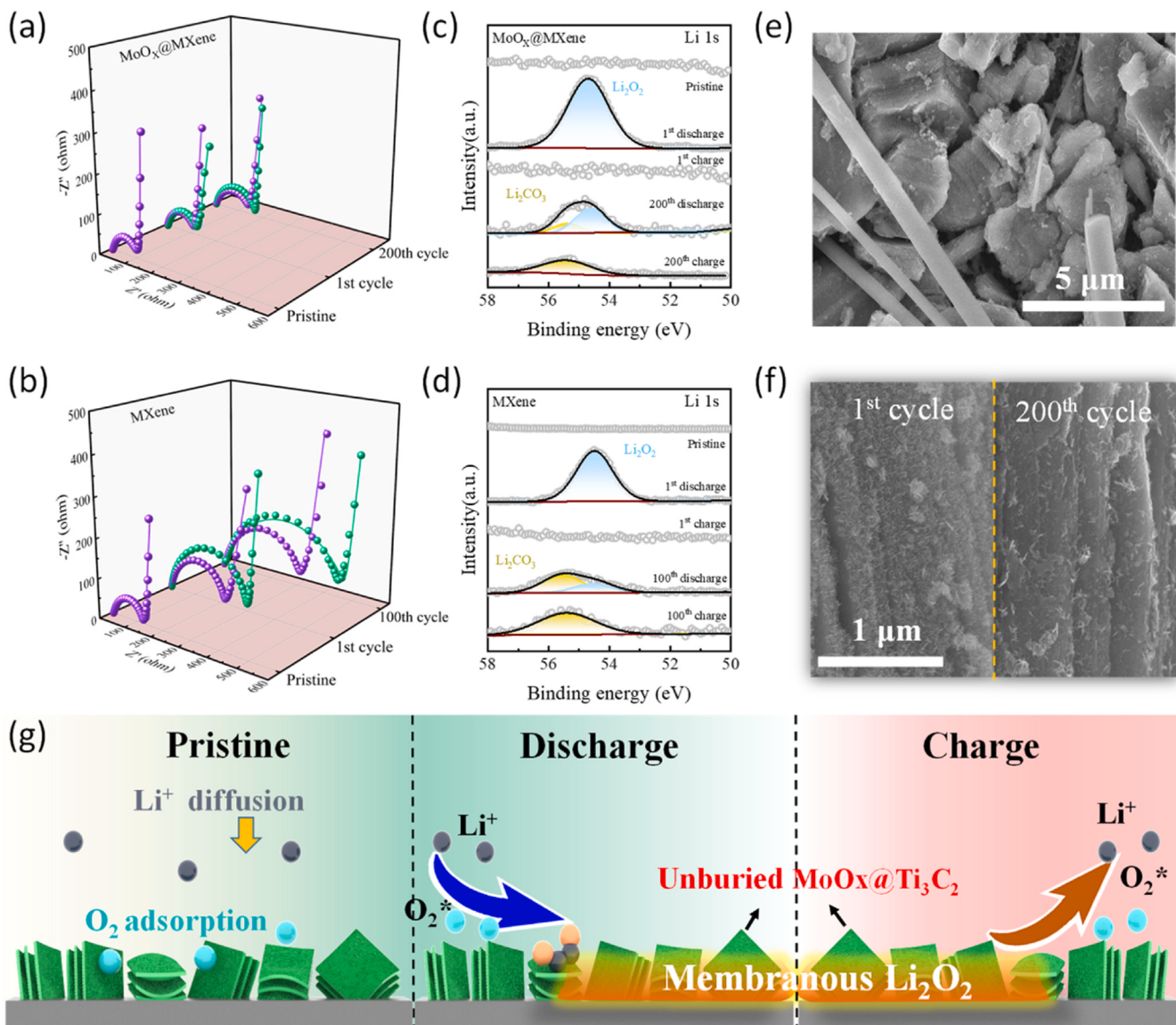


Fig. 4. (a) EIS of $\text{MoO}_x@\text{Ti}_3\text{C}_2$ MXene-based LOBs after different discharge-charge process (Green represents the discharge process and purple represents the charge process); (b) EIS of Ti_3C_2 MXene-based LOBs after different discharge-charge process; (c) Li 1 s of $\text{MoO}_x@\text{Ti}_3\text{C}_2$ MXene at the selected discharge/charge state; (d) Li 1 s of MoO_x at the selected discharge/charge state; (e) SEM images of $\text{MoO}_x@\text{Ti}_3\text{C}_2$ MXene at 200th discharge; (f) SEM images of $\text{MoO}_x@\text{Ti}_3\text{C}_2$ MXene at different charging statuses. (g) Schematic diagram of the reaction during the cycling process in LOBs.

returning to 2500 mA g⁻¹). By comparison, the LOB with Ti₃C₂ MXene catalyst shows relatively serious polarization under ultrahigh rate. Furthermore, the MoO_x@Ti₃C₂ MXene cathode can keep continuously discharge-charge cycling over 250 hrs at 2500 mA g⁻¹ without distinct performance degradation, and even keep a relatively stable overpotential (~2.20 V) after 250 h. However, Ti₃C₂ MXene-based cathode could only maintain less than 50 h and exhibit an increased discharge-charge overpotential from 1.40 V (1st cycle) to 2.71 V (after 50 h cycling), which further revealing the in-situ formation of bimetallic Mo-O-Ti coupling in MoO_x@Ti₃C₂ MXene benefits to effectively optimize the catalytic performance and stability of Ti₃C₂ MXene. The exceptional rate performance of MoO_x@Ti₃C₂ MXene reveals that the MoO_x@Ti₃C₂ MXene-based Li-O₂ battery is provided with the fast charge-discharge characteristics, demonstrating broad practical application prospects. The electrochemical performance of MoO_x@Ti₃C₂ MXene-based LOBs in this work and those of reported typical related catalysts-based LOBs are summarized in Fig. 3h [42–53]. Explicitly, MoO_x@Ti₃C₂ MXene-based LOBs are more competitive than most monomer-based LOBs and in the reported literature and even comparable to MXene-based composite electrocatalysts. The remarkably electrocatalytic performance of MoO_x@Ti₃C₂ MXene catalyst are attributed to their interfacial oxygen bridge bonding with Mo-O-Ti units, unique structure, and reaction dynamics optimization.

3.3. Role of bimetallic-oxygen coupling and catalytic mechanism

To further discover the catalytic mechanism of MoO_x@Ti₃C₂ MXene, electrochemical impedance spectra (EIS) was conducted during the cycling in Fig. 4a and b. The related fitted equivalent circuit is identified in Figure S12, where R₀, CPE, R_{ct}, and W₀ represent the solution resistance, double-layer capacitance, charge-transfer resistance, and Warburg impedance, respectively. The emerging CPE and R_{ct} after discharging suggest a new interface corresponded to the formation of discharge products. The impedance (R_{ct}) of MoO_x@Ti₃C₂ MXene-based cathode exhibits a minimal increase from 125.37 (1st discharge) to 167.59 ohms (200th discharge). Conversely, there is a pronounced increase in R_{ct} of Ti₃C₂ MXene-based cathode (from 297.52 after 1st discharge to 448.93 ohms after 100th discharge), indicating that there is a large accumulation of by-products with low conductivity on the surface of monomeric Ti₃C₂ MXene-based cathode. The EIS analysis reveals that the MoO_x@Ti₃C₂ MXene catalyst is conducive to promote ORR/OER kinetics.

The morphology transformation and composition analysis of catalyst-based cathodes in different cycling were checked out by ex-situ XPS and SEM. As shown in Figure S13, there is almost on obvious difference in the Ti 2p patterns between the pristine state and cycling state for MoO_x@Ti₃C₂ MXene. The ex-situ XPS analysis confirms that MoO_x@Ti₃C₂ MXene delivers good structural stability during the cycling process in LOBs. As demonstrated in Fig. 4c, the peak at 54.7 eV is assigned to the formation of Li₂O₂ on MoO_x@Ti₃C₂ MXene, which could be completely break down during the subsequent charging process. Moreover, the emerging weak peak centra at 55.4 eV correspond to Li₂CO₃ by-product after the 200th discharge, resulting from the undesirable decomposition of the electrolyte at high charging voltage. In contrast, the Li₂CO₃ by-product is irresolvable and insulation during the following cycling, which is consistent with previous EIS analysis. However, a large amount of non-decomposable Li₂CO₃ by-products continuously accumulate on the Ti₃C₂ MXene at the 100th cycle (Fig. 4d), leading to a sharp increase in impedance of LOBs.

From the SEM image in Fig. 4e, membranous Li₂O₂ are formed and uniformly loaded on MoO_x@Ti₃C₂ MXene after discharge. As be widely proven, the morphology of Li₂O₂ is ruled by the electrochemical reaction path of LiO₂. Intermediate products on the electrocatalyst surface. Particularly, the thick films structure of Li₂O₂ adhere to surface-mediated growth principle for * LiO₂(* represents adsorptive state) deposition and strong affinity with MoO_x@Ti₃C₂ MXene catalyst [54].

Defer from traditional toroidal-like Li₂O₂, membranous Li₂O₂ delivers better Li₂O₂/ MoO_x@Ti₃C₂ multiphase interface with enhanced ORR/OER dynamic [55]. Besides, the distinctive nanosheets structure of MoO_x would not be completely covered up by membranous Li₂O₂ (Fig. 4f), exposing abundant active sites to facilitate the following decomposition of Li₂O₂. Surprisingly, MoO_x could maintain nanosheets structure after long-term cycling. Thus, the gradually raised voltage polarization and performance degradation of LOBs are largely consequent on the serious decomposition of organic electrolytes, rather than the not incompletely passivated MoO_x@Ti₃C₂ MXene-based cathode. Substantially, as graphically shown in Fig. 4g, the in-situ generated discharge products Li₂O₂ will not completely enshroud the highly catalytic active sites of MoO_x@Ti₃C₂, allowing for complete decomposition of Li₂O₂ during the subsequent charging process.

The intrinsic role of bimetallic-oxygen coupling in improving LOBs performance is rationalized by density functional theory (DFT). The Mo tends to bond with O from TiO_x active layer in MoO_x@Ti₃C₂ MXene (Fig. 5a), leading to lower charge adsorption ability of Mo. The modified charge distribution around the bimetallic-oxygen coupling could influence the diffusion rate of ions and optimize the formation path of Li₂O₂. Moreover, Fig. 5b confirms that MoO_x@Ti₃C₂ MXene exhibits an exceptional metallic conductor character, while Ti₃C₂ MXene behaves as a semiconductor with little bandgap. By comparison, the uniformly loaded MoO_x nanoparticles and in-situ generated bimetallic-oxygen coupling can effectively decorate electronic property and thereby boost the conductivity and catalytic performance of MoO_x@Ti₃C₂ MXene (Figure S14 and Figure S15). The atomic level reaction steps of discharge products on MoO_x@Ti₃C₂ MXene and Ti₃C₂ MXene are calculated and analyzed in Fig. 5c and d. MoO_x@Ti₃C₂ MXene shows lower free energy under open circuit state (U = 0 V), indicating a smaller impedance in MoO_x@Ti₃C₂ MXene-based LOBs. Besides, the bimetallic-oxygen coupling in MoO_x@Ti₃C₂ MXene delivers the lower binding free energy of *LiO₂ (-3.21 eV) than that of mono Ti-O bonding in Ti₃C₂ MXene (-4.00 eV), manifesting a better ORR dynamics optimization of MoO_x@Ti₃C₂ MXene-based LOBs. The higher ORR catalytic activity of MoO_x@Ti₃C₂ MXene catalyst is owing to the electron-withdrawing effect of Ti centers regulate by bimetallic-oxygen coupling, which reduced the electron density as well as the binding barrier with *LiO₂. In addition, the better electronic capture capability of Ti centers leads to LiO₂ preferentially adsorbing on the surface of titanium oxide rather than molybdenum oxide in MoO_x@Ti₃C₂ MXene, resulting to the incomplete coverage of Li₂O₂ on the MoO_x nanosheets which could be the main catalytic sites for promoting the subsequent Li₂O₂ decomposition. As displayed in Figure S16, MoO_x@Ti₃C₂ MXene catalyst delivers stronger binding interactions with LiO₂, with adsorption energies of -4.84, which is bigger than that of Ti₃C₂ MXene (-3.72). The more negative adsorption energy implies MoO_x@Ti₃C₂ MXene show stronger interaction with intermediate products LiO₂. Thus, these DFT analysis reveals that the presence of interfacial oxygen bridge bonding with Mo-O-Ti units can improve the adsorption ability of whole catalyst, promoting the oxidation activity of LiO₂ on MoO_x@Ti₃C₂ MXene surface.

4. Conclusion

In summary, a bimetallic-oxygen coupling with good oxygen redox dynamics optimization in MoO_x@Ti₃C₂ MXene has been well originated and further applied as cathode catalyst for LOBs. The combination of MoO_x and Ti₃C₂ MXene guaranteed by Ti-O-Mo units could induce the composite with unique morphology, extraordinary ultrahigh-rate stability, favourable electronic structure, and quality electrocatalytic activity. LOBs with the MoO_x@Ti₃C₂ MXene catalyst deliver a low overpotential of 0.75 V and stable lifespan of over 300 cycles at ultrahigh current density of 2500 mA g⁻¹. Ex-situ DFT theory and experimental analysis confirm the critical role of bimetallic-oxygen coupling in maximize the advantages of electronic structural regulation and controlling the Li₂O₂ formation mode. This work could highlight the

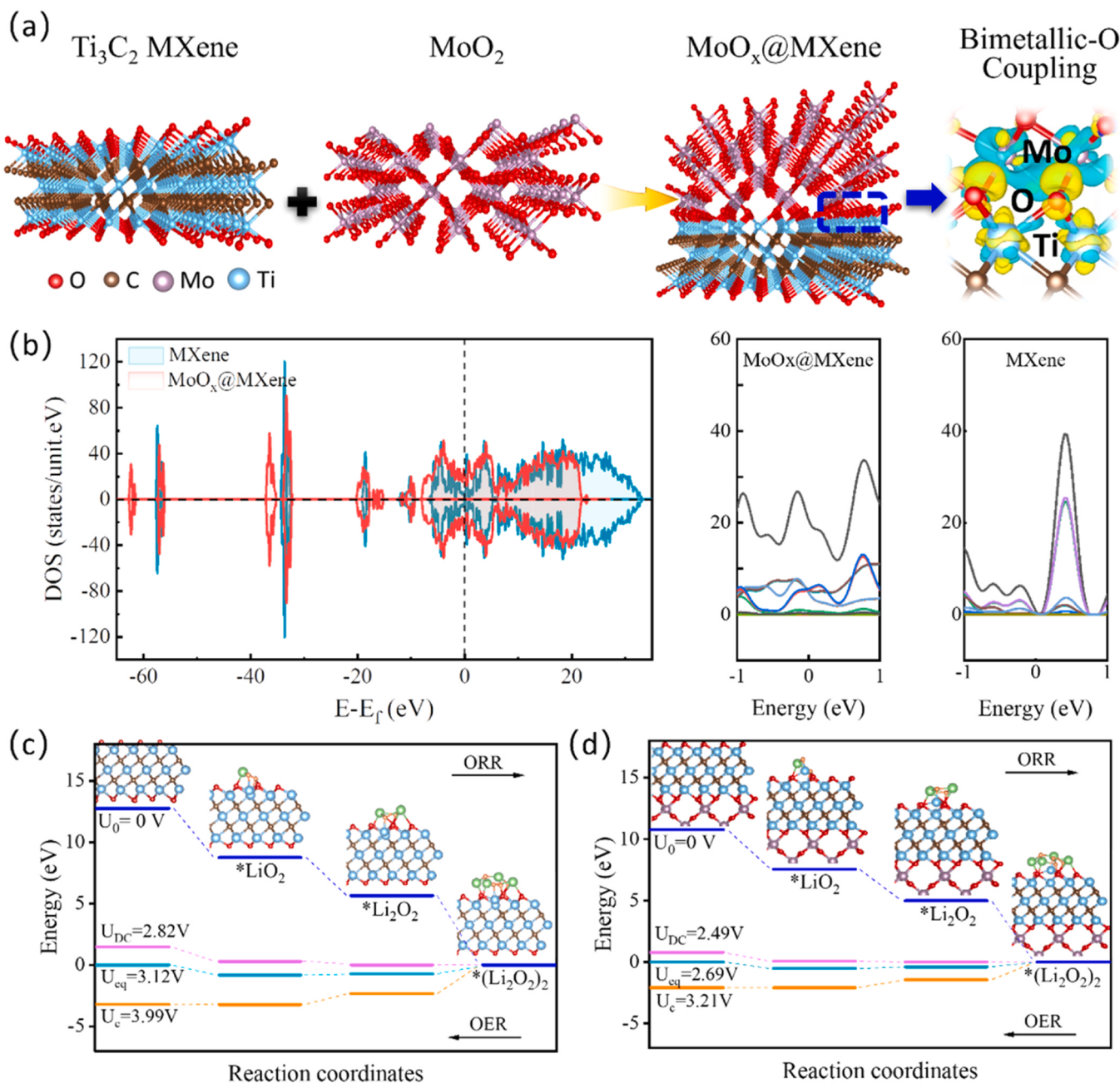


Fig. 5. (a) Schematic structure description of the bimetallic-oxygen coupling in $\text{MoO}_x@\text{Ti}_3\text{C}_2$ MXene. (b) Electronic density of states (DOS) for the bulk structure of $\text{MoO}_x@\text{Ti}_3\text{C}_2$ MXene and Ti_3C_2 MXene. Free energy diagrams of battery reactions on the surface of TiO_x in Ti_3C_2 MXene (c) and the bimetallic-oxygen coupling in $\text{MoO}_x@\text{Ti}_3\text{C}_2$ MXene (d).

enormous prospects of bimetallic-oxygen coupling in the practical design of significant MXene-based cathode catalyst for LOBs.

CRediT authorship contribution statement

Jixiong Zhang: Writing – review & editing, Supervision, Funding acquisition, Conceptualization. **Nan Zhou:** Methodology. **Meng Li:** Visualization, Investigation. **Hengfeng Liu:** Validation. **Zhihui Sun:** Writing – original draft, Data curation, Conceptualization. **Yingjie Hu:** Visualization, Methodology. **Binbin Huo:** Validation, Methodology. **Ming Chao:** Writing – review & editing, Supervision. **Zeng Kai:** Writing – review & editing, Supervision, Conceptualization.

Declaration of Competing Interest

This work has not been published in whole or in part elsewhere. This paper is not currently being considered for publication elsewhere. The publication is approved by all authors and tacitly or explicitly by the responsible authorities where the work was carried out.

If accepted, it will not be published elsewhere in the same form, in English or in any other language, without the written consent of the Published.

Data availability

Data will be made available on request.

Acknowledgements

This work was supported by the National Natural Science Foundation of China (52304161), the Fundamental Research Funds for the Central Universities (2022QN1003, 2682023CX006), the Key R&D Program of Xinjiang Uygur Autonomous Region (2023B01009), and the China Postdoctoral Science Foundation (2021M703495). We are grateful to the Excellent Science and Technology Innovation Group of Jiangsu Province for providing accurate theoretical calculation analysis. Zhihui Sun and Yingjie Hu contributed equally to this work.

Appendix A. Supporting information

Supplementary data associated with this article can be found in the online version at doi:10.1016/j.apcatb.2024.123984.

References

- [1] M.M. Ottakam Thotiyil, S.A. Freunberger, Z. Peng, Y. Chen, Z. Liu, P.G. Bruce, A stable cathode for the aprotic Li-O₂ battery, *Nat. Mater.* 12 (2013) 1050–1056.
- [2] C. Zhao, Z. Yan, B. Zhou, Y. Pan, A. Hu, M. He, J. Liu, J. Long, Identifying the role of Lewis-base sites for the chemistry in lithium-oxygen batteries, *Angew. Chem. Int. Ed.* 62 (2023) e202302746.
- [3] S.T. Plunkett, A. Kondori, D.Y. Chung, J. Wen, M. Wolfman, S.H. Lapidus, Y. Ren, R. Amine, K. Amine, A.U. Mane, M. Asadi, S. Al-Hallaj, B.P. Chaplin, K.C. Lau, H.-W. Wang, L.A. Curtiss, A new cathode material for a Li-O₂ battery based on lithium superoxide, *ACS Energy Lett.* 7 (2022) 2619–2626.
- [4] R. Jiang, T. Naren, Y. Chen, Z. Chen, C. Zhang, L. Ma, H. Xu, L. Chen, L. Zhou, W. Wei, A dual-functional circular organic small molecule for dendrite-free zinc metal batteries with long-term cycling, *Energy Storage Mater.* 63 (2023) 103044.
- [5] H. Wang, X. Wang, M. Li, L. Zheng, D. Guan, X. Huang, J. Xu, J. Yu, Porous materials applied in nonaqueous Li-O₂ batteries: status and perspectives, *Adv. Mater.* 32 (2020) 2002559.
- [6] Y. Zhao, W. Cheng, J. Wu, Z. Hu, F. Liu, L. Wang, H. Peng, Recent advances in charge mechanism of noble metal-based cathodes for Li-O₂ batteries, *Chin. Chem. Lett.* 34 (2023) 107413.
- [7] Q. Qiu, J. Long, P. Yao, J. Wang, X. Li, Z.-Z. Pan, Y. Zhao, Y. Li, Cathode electrocatalyst in aprotic lithium oxygen (Li-O₂) battery: a literature survey, *Catal. Today* 420 (2023) 114138.
- [8] B.Y. Xu, T.Y. Liu, X.C. Liang, W.J. Dou, H.B. Geng, Z.Y. Yu, Y.F. Li, Y. Zhang, Q. Shao, J.M. Fan, X.Q. Huang, Pd-Sb rhombohedra with an unconventional rhombohedral phase as a trifunctional electrocatalyst, *Adv. Mater.* 34 (2022) 2206528.
- [9] L.F. Ren, R.X. Zheng, D.Y. Du, Y. Yan, M. He, Z.Q. Ran, M.L. Li, C.Z. Shu, Optimized orbital occupancy of transition metal in spinel Ni-Co oxides with heteroatom doping for Aprotic Li-O₂ battery, *Chem. Eng. J.* 430 (2022).
- [10] D. Cao, L.M. Zheng, Q.J. Li, J.F. Zhang, Y. Dong, J.S. Yue, X.R. Wang, Y. Bai, G. Q. Tan, C. Wu, Crystal phase-controlled modulation of binary transition metal oxides for highly reversible Li-O₂ batteries, *Nano Lett.* 21 (2021) 5225–5232.
- [11] Z. Liu, Z.W. Zhao, W. Zhang, Y. Huang, Y. Liu, D.A.L. Wu, L. Wang, S.L. Chou, Toward high-performance lithium-oxygen batteries with cobalt-based transition metal oxide catalysts: advanced strategies and mechanical insights, *Infomat* 4 (2022) e12260.
- [12] L.J. Zheng, Y. Yan, X.X. Wang, L.N. Song, H.F. Wang, J.J. Xu, Regulating electrochemistry kinetics and discharge product selectivity with near-free cobalt single-atom catalyst in Li-O₂ batteries, *Energy Storage Mater.* 56 (2023) 331–341.
- [13] Y. Wu, Y. Wang, R. Chen, J. Xu, Y. Wang, H. Zhang, Y. Ding, B. Li, S. Dong, S. Dou, X. Zhang, J. Sun, J. Sun, On-site catalytic wastewater remediation by sustainably produced H₂O₂ via scalable single-atomic Fe-incorporated Janus membrane, *Appl. Catal. B: Environ.* 343 (2024) 123533.
- [14] Y. Ding, T. Yan, J. Wu, M. Tian, M. Lu, C. Xu, J. Gu, H. Zhao, Y. Wang, X. Pan, S. Dou, L. Zhang, J. Sun, Imparting selective polysulfide conversion via geminal-atom moieties in lithium-sulfur batteries, *Appl. Catal. B: Environ.* 343 (2024) 123553.
- [15] D. Cao, Y. Bai, J.F. Zhang, G.Q. Tan, C.A. Wu, Irreplaceable carbon boosts Li-O₂ batteries: From mechanism research to practical application, *Nano Energy* 89 (2021).
- [16] H.B. Chen, Y.Q. Ye, X.Z. Chen, L.L. Zhang, G.X. Liu, S.Q. Wang, L.X. Ding, N-doped porous carbon nanofibers inlaid with hollow Co₃O₄ nanoparticles as an efficient bifunctional catalyst for rechargeable Li-O₂ batteries, *Chin. J. Catal.* 43 (2022) 1511–1519.
- [17] L. Shi, Z. Li, Y.P. Li, G. Wang, M.F. Wu, Z.Y. Wen, Suppressing redox shuttle with MXene-modified separators for Li-O₂ batteries, *ACS Appl. Mater. Interfaces* 13 (2021) 30766–30775.
- [18] X. Zheng, M. Yuan, Y. Zhao, Z. Li, K. Shi, H. Li, G. Sun, Status and prospects of MXene-based lithium-oxygen batteries: theoretical prediction and experimental modulation, *Adv. Energy Mater.* 13 (2023) 2204019.
- [19] X. Zheng, M. Yuan, D. Guo, C. Wen, X. Li, X. Huang, H. Li, G. Sun, Theoretical design and structural modulation of a surface-functionalized Ti₃C₂T_x MXene-based heterojunction electrocatalyst for a Li-oxygen battery, *ACS Nano* 16 (2022) 4487–4499.
- [20] X. Li, C. Wen, H. Li, G. Sun, In situ decoration of nanosized metal oxide on highly conductive MXene nanosheets as efficient catalyst for Li-O₂ battery, *J. Energy Chem.* 47 (2020) 272–280.
- [21] J. Li, F. Zeng, J.K. El-Demellawi, Q. Lin, S. Xi, J. Wu, J. Tang, X. Zhang, X. Liu, S. Tu, Nb₂CT_x MXene cathode for high-capacity rechargeable aluminum batteries with prolonged cycle lifetime, *ACS Appl. Mater. Interfaces* 14 (2022) 45254–45262.
- [22] Q. Ma, Z. Zhang, P. Kou, D. Wang, Z. Wang, H. Sun, R. Zheng, Y. Liu, In-situ synthesis of niobium-doped TiO₂ nanosheet arrays on double transition metal MXene (TiNbCT_x) as stable anode material for lithium-ion batteries, *J. Colloid Interf. Sci.* 617 (2022) 147–155.
- [23] Z. Sun, S. Zhao, J. Zhang, High-conductive multilayer TiO_x-Ti₃C₂T_x electrocatalyst for longevous metal-oxygen battery under a high rate, *Batteries* 9 (2023) 205.
- [24] Y. Jiang, M. Tian, H. Wang, C. Wei, Z. Sun, M.H. Rummeli, P. Strasser, J. Sun, R. Yang, Mildly oxidized MXene (Ti₃C₂, Nb₂C, and V₂C) electrocatalyst via a generic strategy enables longevous Li-O₂ battery under a high rate, *ACS Nano* 15 (2021) 19640–19650.
- [25] D. Cao, L.M. Zheng, Y.H. Wang, Y. Dong, Q.J. Li, Y. Li, X.R. Wang, Y. Bai, G.Q. Tan, C. Wu, Ultraviolet-assisted construction of low-Pt-loaded MXene catalysts for high-performance Li-O₂ batteries, *Energy Storage Mater.* 51 (2022) 806–814.
- [26] A. Lee, D. Krishnamurthy, V. Viswanathan, Exploring MXenes as cathodes for non-aqueous lithium-oxygen batteries: design rules for selectively nucleating Li₂O₂, *Chemsuschem* 11 (2018) 1911–1918.
- [27] X.C. Cao, X.J. Zheng, Z.H. Sun, C. Jin, J.H. Tian, S.R. Sun, R.Z. Yang, Oxygen defect-ridden molybdenum oxide-coated carbon catalysts for Li-O₂ battery cathodes, *Appl. Catal. B: Environ.* 253 (2019) 317–322.
- [28] M. Rittirum, P. Buapin, T. Saelee, P. Khajondetchairit, S. Kheawhom, B. Alling, S. Prasertthdam, A. Ektarawong, P. Prasertthdam, First-principles calculation on effects of oxygen vacancy on α -MnO₂ and β -MnO₂ during oxygen reduction reaction for rechargeable metal-air batteries, *J. Alloy. Compd.* 926 (2022) 166929.
- [29] Z. Sun, Y. Hu, K. Zeng, M. Li, S. Zhao, J. Zhang, Turn "Waste" into wealth: MoO₂@coal gangue electrocatalyst with amorphous/crystalline heterostructure for efficient Li-O₂ batteries, *Small* 19 (2023) 2208145.
- [30] X. Xie, X. Zhang, W. Tian, X. Zhang, J. Ding, Y. Liu, S. Lu, Tri-functional Ru-RuO₂/Mn-MoO₂ composite: a high efficient electrocatalyst for overall water splitting and rechargeable Zn-air batteries, *Chem. Eng. J.* 468 (2023) 143760.
- [31] H. Xu, N. Liang, L. Cui, H. Zhang, B. Yang, Z. Jin, Synergistic effect of interface and defect engineering of MoC/MoO₂ nano dot encapsulated N-doped carbon nanoflowers for highly durable dye-sensitized solar cells, *J. Colloid Interface Sci.* 653 (2024) 1620–1629.
- [32] X.C. Cao, Z.H. Sun, X.J. Zheng, C. Jin, J.H. Tian, X.W. Li, R.Z. Yang, MnCo₂O₄/MoO₂ nanosheets grown on ni foam as carbon- and binder-free cathode for lithium-oxygen batteries, *Chemsuschem* 11 (2018) 574–579.
- [33] S.P. Zhang, G. Wang, J. Jin, L.L. Zhang, Z.Y. Wen, J.H. Yang, Self-catalyzed decomposition of discharge products on the oxygen vacancy sites of MoO₃ nanosheets for low-overpotential Li-O₂ batteries, *Nano Energy* 36 (2017) 186–196.
- [34] L. Gurusamy, L. Karuppasamy, S. Anandan, C.-H. Liu, J.J. Wu, Defective engineering of heterostructured N-Mo₂C@MoO_{3-x} electrode materials for the dual function of electrochemical sensing and supercapacitor applications, *Electrochim. Acta* 408 (2022) 139964.
- [35] X. Liu, K. Deng, P. Liu, X. Lv, W. Tian, K. Ma, H. Li, J. Ji, Mutual promotion by structural design and intrinsic activity coupling of CNTs/MoC/CoNiMo for water splitting and urea electrolysis, *Appl. Catal. B: Environ.* 343 (2024) 123470.
- [36] D. Vanderbilt, Soft self-consistent pseudopotentials in a generalized eigenvalue formalism, *Phys. Rev. B* 41 (1990) 7892.
- [37] Y. Zhang, S. Zhang, J. Ma, A. Huang, M. Yuan, Y. Li, G. Sun, C. Chen, C. Nan, Oxygen vacancy-rich RuO₂-Co₃O₄ nanohybrids as improved electrocatalysts for Li-O₂ batteries, *ACS Appl. Mater. Interfaces* 13 (2021) 39239–39247.
- [38] X. Mu, C. Xia, B. Gao, S. Guo, X. Zhang, J. He, Y. Wang, H. Dong, P. He, H. Zhou, Two-dimensional Mo-based compounds for the Li-O₂ batteries: catalytic performance and electronic structure studies, *Energy Storage Mater.* 41 (2021) 650–655.
- [39] T. Gejo, K. Okada, T. Ibuki, Photoabsorption spectrum of ozone in the K-edge region, *Chem. Phys. Lett.* 277 (1997) 497–501.
- [40] W. Wang, L. Huai, S. Wu, J. Shan, J. Zhu, Z. Liu, L. Yue, Y. Li, Ultrahigh-volumetric-energy-density lithium–sulfur batteries with lean electrolyte enabled by cobalt-doped MoS₂/Ti₃C₂T_x MXene bifunctional catalyst, *ACS Nano* 15 (2021) 11619–11633.
- [41] H. Yin, Z. Chen, Y. Peng, S. Xiong, Y. Li, H. Yamashita, J. Li, Dual active centers bridged by oxygen vacancies of ruthenium single-atom hybrids supported on molybdenum oxide for photocatalytic ammonia synthesis, *Angew. Chem. Int. Ed.* 61 (2022) e202114242.
- [42] C. Wu, Y. Hou, J. Jiang, H. Guo, H. Liu, J. Chen, J. Wang, Heterostructured Mo₂C-MoO₂ as highly efficient catalyst for rechargeable Li-O₂ battery, *J. Power Sources* 470 (2020) 228317.
- [43] P. Wang, D. Zhao, X. Hui, Z. Qian, P. Zhang, Y. Ren, Y. Lin, Z. Zhang, L. Yin, Bifunctional catalytic activity guided by rich crystal defects in Ti₃C₂ MXene quantum dot clusters for Li-O₂ batteries, *Adv. Energy Mater.* 11 (2021) 2003069.
- [44] D. Zhao, P. Wang, H. Di, P. Zhang, X. Hui, L. Yin, Single semi-metallic selenium atoms on Ti₃C₂ MXene nanosheets as excellent cathode for lithium–oxygen batteries, *Adv. Funct. Mater.* 31 (2021) 2010544.
- [45] X. Li, C. Wen, M. Yuan, Z. Sun, Y. Wei, L. Ma, H. Li, G. Sun, Nickel oxide nanoparticles decorated highly conductive Ti₃C₂ MXene as cathode catalyst for rechargeable Li-O₂ battery, *J. Alloy. Compd.* 824 (2020) 153803.
- [46] R. Zheng, C. Shu, Z. Hou, A. Hu, P. Hei, T. Yang, J. Li, R. Liang, J. Long, Situ fabricating oxygen vacancy-rich TiO₂ nanoparticles via utilizing

thermodynamically metastable Ti atoms on $Ti_3C_2T_x$ MXene nanosheet surface to boost electrocatalytic activity for high-performance Li-O₂ batteries, *ACS Appl. Mater. Interfaces* 11 (2019) 46696–46704.

[47] C.-S. Yang, Z. Sun, Z. Cui, F.-L. Jiang, J.-W. Denga, T. Zhang, Inward growth of superthin TiC skin on carbon nanotube framework as stable cathode support for Li-O₂ batteries, *Energy Storage Mater.* 30 (2020) 59–66.

[48] S. Zhang, G. Wang, J. Jin, L. Zhang, Z. Wen, J. Yang, Self-catalyzed decomposition of discharge products on the oxygen vacancy sites of MoO₃ nanosheets for low-overpotential Li-O₂ batteries, *Nano Energy* 36 (2017) 186–196.

[49] G. Li, N. Li, S. Peng, B. He, J. Wang, Y. Du, W. Zhang, K. Han, F. Dang, Highly efficient Nb₂C MXene cathode catalyst with uniform O-terminated surface for lithium-oxygen batteries, *Adv. Energy Mater.* 11 (2021) 2002721.

[50] X. Cao, X. Zheng, Z. Sun, C. Jin, J. Tian, S. Sun, R. Yang, Oxygen defect-ridden molybdenum oxide-coated carbon catalysts for Li-O₂ battery cathodes, *Appl. Catal. B: Environ.* 253 (2019) 317–322.

[51] H. Xu, R. Zheng, D. Du, L. Ren, R. Li, X. Wen, C. Zhao, C. Shu, V₂C MXene enriched with -O termination as high-efficiency electrocatalyst for lithium-oxygen battery, *Appl. Mater. Today* 27 (2022) 101464.

[52] J. Li, K. Han, J. Huang, G. Li, S. Peng, N. Li, J. Wang, W. Zhang, Y. Du, Y. Fan, W. Wang, F. Dang, Polarized nucleation and efficient decomposition of Li₂O₂ for Ti₂C MXene cathode catalyst under a mixed surface condition in lithium-oxygen batteries, *Energy Storage Mater.* 35 (2021) 669–678.

[53] M. Wu, D.Y. Kim, H. Park, K.M. Cho, J.Y. Kim, S.J. Kim, S. Choi, Y. Kang, J. Kim, H. T. Jung, Formation of toroidal Li₂O₂ in non-aqueous Li-O₂ batteries with Mo₂CT_x MXene/CNT composite, *RSC Adv.* 9 (2019) 41120–41125.

[54] C. Yang, R.A. Wong, M. Hong, K. Yamanaka, T. Ohta, H.R. Byon, Unexpected Li₂O₂ film growth on carbon nanotube electrodes with CeO₂ nanoparticles in Li-O₂ batteries, *Nano Lett.* 16 (2016) 2969–2974.

[55] Y. Li, R. Zhang, B. Chen, N. Wang, J. Sha, L. Ma, D. Zhao, E. Liu, S. Zhu, C. Shi, N. Zhao, Induced construction of large-area amorphous Li₂O₂ film via elemental co-doping and spatial confinement to achieve high-performance Li-O₂ batteries, *Energy Storage Mater.* 44 (2022) 285–295.